



# Sono-synthesis of bismuth ferrite nanoparticles with high photocatalytic activity in degradation of Rhodamine B under solar light irradiation



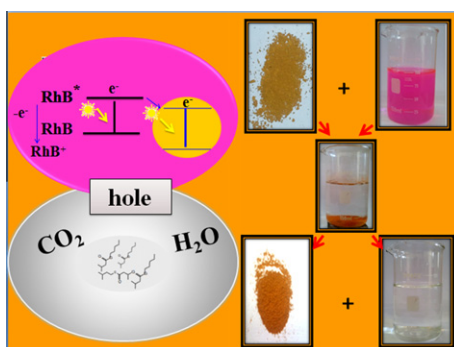
Tayyabe Soltani, Mohammad H. Entezari\*

Department of Chemistry, Ferdowsi University of Mashhad, 91775 Mashhad, Iran

## HIGHLIGHTS

- BiFeO<sub>3</sub> was synthesized in mild conditions with ultrasound.
- Rhodamine B was completely destroyed in 35 min under sunlight irradiation.
- Complete mineralization was achieved in 90 min.
- BiFeO<sub>3</sub> had no significant loss of activity even after four cycles of uses.
- Hole had a main role in photocatalytic degradation of RhB.

## GRAPHICAL ABSTRACT



## ARTICLE INFO

### Article history:

Received 7 January 2013  
Received in revised form 25 February 2013  
Accepted 27 February 2013  
Available online 8 March 2013

### Keywords:

BiFeO<sub>3</sub>  
Ultrasound  
RhB  
Photodegradation  
Sunlight

## ABSTRACT

In this work, pure bismuth ferrite (BiFeO<sub>3</sub>) as a visible-light photocatalyst has successfully synthesized via ultrasonic method in a short time and low temperature. The product was characterized by different techniques. Then, the degradation of Rhodamine B (RhB) was investigated under sunlight irradiation by bismuth ferrites synthesized with ultrasound. The RhB in solution was completely degraded in 35 min under applied conditions in acidic medium. The nanocatalyst did not exhibit significant loss of activity even after four cycles of successive uses. The total organic carbon (TOC) measurements displayed a complete mineralization in 90 min. To determine the mechanism of photocatalytic degradation of RhB, different methods were used. Based on the results, two possible competitive photodegradation pathways proposed: chromophores cleavage and N-deethylation. The hole as a reactive species had a key role in the degradation process. The BiFeO<sub>3</sub> (BFO) nanoparticles synthesized with ultrasound exhibited higher crystallization, smaller crystallite size and a higher photocatalytic activity than the sample synthesized with sol–gel method in stricter conditions.

© 2013 Elsevier B.V. All rights reserved.

## 1. Introduction

Degradation of the dyes in industrial wastewaters has generated considerable attention due to their huge volume of production, slow biodegradation, low decoloration and high toxicity [1]. In addition of azo dyes, the degradation of triphenylmethane dyes has been investigated previously [2–4].

During the dyeing process, nearly 1–20% of the total world production of dyes is released in the textile effluents [5,6]. Rhodamine B (RhB) is a typical cationic dye with high solubility in water and has been broadly used as a colorant food and in textile industries.

Today, photocatalysis was proved to be as an excellent method over than others due to the use of oxygen as an oxidant, oxidation of the organic compounds at low temperatures and even at low concentrations, and complete mineralization. TiO<sub>2</sub> is used for the degradation of many organic compounds under UV irradiation. Approximately, less than 4% of solar spectrum includes the UV

\* Corresponding author. Fax: +98 511 8795457.

E-mail address: [moh\\_Entezari@yahoo.com](mailto:moh_Entezari@yahoo.com) (M.H. Entezari).

irradiation, while more than 50% is visible light. Hence, development of non-titania semiconductors with strong absorbance in the visible region is very important [7–9].

Perovskite-type BiFeO<sub>3</sub> (BFO) is known as one of the several compounds that demonstrates the coexistence of ferroelectric and antiferromagnetic orders above room temperature with Neel temperature ( $T_N \sim 375^\circ\text{C}$ ) and Curie temperature ( $T_C \sim 830\text{--}850^\circ\text{C}$ ) [10]. Also, nanopowder shows a weak ferromagnetic (FM) order at room temperature which is quite different from the linear magnetization–magnetic field relationship in the bulk [11].

In addition to the potential magnetoelectric applications, it exhibits applications as a visible light photocatalyst due to its narrow band-gap energy (2.1 eV), high chemical stability during the photocatalytic process, and as multiferric compound [12]. The photocatalytic activity of BFO has been reported before by others [13–17].

The fabrication of BFO by different methods often is complex and performs at high temperatures which lead to impurity phases such as Bi<sub>2</sub>O<sub>3</sub>, Fe<sub>2</sub>O<sub>3</sub>, and Bi<sub>2</sub>Fe<sub>4</sub>O<sub>9</sub> [18,19].

In order to eliminate these limitations, ultrasound can be used as an energy source. Sonochemistry has been successfully used for the fabrication and modification of nanosized functional inorganic materials [20]. The chemical effects of ultrasound arise from acoustic cavitations that are the formation, growth and collapse of the bubbles in liquid [21].

The recent works has been done in our lab confirmed that the ultrasound has a critical role in the synthesis of crystalline nanomaterials [22–25], degradation of dye [26,27] and also photocatalytic degradation of the dye [28,29].

In this work, ultrasound has been applied in the preparation of BFO nanoparticles for the photocatalytic applications. The sonosynthesis of BFO nanoparticles were carried out in a short time under mild conditions. The complete degradation of RhB was approved in the presence of BFO nanoparticles under direct solar light irradiation.

## 2. Materials and methods

### 2.1. Chemical and materials

Bismuth nitrate (Bi(NO<sub>3</sub>)<sub>3</sub>·5H<sub>2</sub>O), Iron nitrate (Fe(NO<sub>3</sub>)<sub>3</sub>·9H<sub>2</sub>O) and Ethylene glycol (EG) from Merck have been used without further purification. RhB from Aldrich, were used as received. Ethanol, T-butyl alcohol and Potassium iodides were analytical reagent grade and used without further purification and de-ionized water were used for the sample preparation.

### 2.2. Preparation of BFO

First, 0.008 mol of Bi(NO<sub>3</sub>)<sub>3</sub>·5H<sub>2</sub>O, in EG was sonicated for 15 min to form a transparent solution. The initial temperature was 9 °C and it was reached to 35 °C during the sonication and in case of without ultrasound, it lasts 2.5 h at 35 °C. Second, stoichiometric proportion of Fe(NO<sub>3</sub>)<sub>3</sub>·9H<sub>2</sub>O was added into the solution. The mixture was sonicated for another 5 min at the same temperature to obtain a brownish red sol. This step without sonication was stirred for 1 h. Then the samples were kept at 70 °C to form a xerogel. The obtained powders were calcinated at different temperatures (400 and 500 °C for 0.5 h). Finally, the powders washed with distilled water and absolute alcohol for several times and dried at 70 °C.

### 2.3. Characterization and equipment

The Fourier-transformed infrared spectroscopy (FT-IR, Avatar 370) using the KBr pellet method were recorded on a Thermo-Nicolet spectrometer and the crystalline structure was identified by X-ray diffraction (XRD, Philips PW1800) employing Cu K $\alpha$  ( $\lambda = 1.5406 \text{ \AA}$ ,

$2\theta = 10\text{--}70^\circ$ ). The samples' morphology and size were examined with scanning electron microscope (SEM, VP 1450 LEO) and transmission electron microscope (TEM, Leo 912 AB). The magnetization of the product was measured with vibrating sample magnetometer (VSM, HH-20) operating at ambient temperatures. The light absorption ability was analyzed by UV–vis diffuse reflectance spectra (DRS, MC-2530). Thermogravimetric analysis and differential thermal analysis (TGA/DTA, Shimadzu TA-50) were carried out in air from 30 to 1000 °C at a heating rate of 10 °C min<sup>-1</sup>. The absorption spectrum of RhB was measured using a UV–vis spectrophotometer (Unico 2800). The total organic carbon (TOC, Shimadzu) was determined by TOC-V CPH. Gas chromatography/mass spectrometry analysis (GC/MS, QP2010 with column RT X-5MS) was carried out for clarification the temporal course of the reaction.

The point of zero charge (PZC) of the sample was determined by plotting the final pH versus the initial pH [30]. The intercept of this curve with the straight line corresponding to equal pH of initial and final is the pH<sub>PZC</sub> (Fig. S1).

The ultrasonic irradiation was applied with equipment operating at 20 kHz (Branson Digital sonifier, W-450 D).

### 2.4. Activity test

The catalytic activity of BFO nanoparticles has been evaluated for the photocatalytic degradation of RhB in an aqueous solution. In this case, the Pyrex glass vessel containing 100 mL RhB (25 mg L<sup>-1</sup>) and 0.05 g of catalyst at pH 2.5 was magnetically stirred. Several stirrer were used in equal rate of stirring and predetermined time intervals on the window ledge under direct solar radiation in consecutive sunny days in July 2012 between 11 am and 3 pm (GPS coordinates: N = 36°18'41.6", E = 59°31'54.2"). The temperature of the solution was between 28 and 32 °C. Before sunlight irradiation, the solutions were magnetically stirred in a dark place to attain adsorption–desorption equilibrium between the dye and photocatalyst. The experiment was carried out in different times and 10 min was required to reach equilibrium.

Different amounts of catalyst (0.20 g L<sup>-1</sup>, 0.50 g L<sup>-1</sup>, 0.75 g L<sup>-1</sup> and 1.00 g L<sup>-1</sup>) were tested (not shown) and the best dosage was selected (0.50 g L<sup>-1</sup>). It should be mentioned that by increasing the amount of catalyst, the turbidity of the suspension was also increased and this led to the decrease of light penetration and light scattering [31]. At given interval times, about 5 mL of suspensions were sampled and separated from the solution with an external magnetic field. The removal of RhB was determined based on the absorption at 553 nm using a UV–vis spectrophotometer. Then, the absorption was converted to concentration through the standard curve of RhB (Fig. S2).

Experiments under different pH were also carried out to reveal the role of pH on the photocatalytic activity of BFO nanoparticles. The pH values were adjusted by adding HCl or NaOH. The desorption test was performed on the surface of BFO after separation from the solution. The separated BFO was dispersed in 100 mL of aqueous solution with pH = 10, then the solution was filtered from the solid phase and the absorption was measured at 553 nm using a UV–vis spectrophotometer.

For identification of the intermediates, after decolorization of RhB for about 40 min, the liquid phase was separated from catalyst by an external magnetic field. Then, the organic phase was extracted for different analyses.

## 3. Results and discussion

### 3.1. Characterization of the catalyst

The FT-IR spectrum of BFO nanoparticles synthesized with ultrasound is shown in Fig. S3. The broad band between 3000

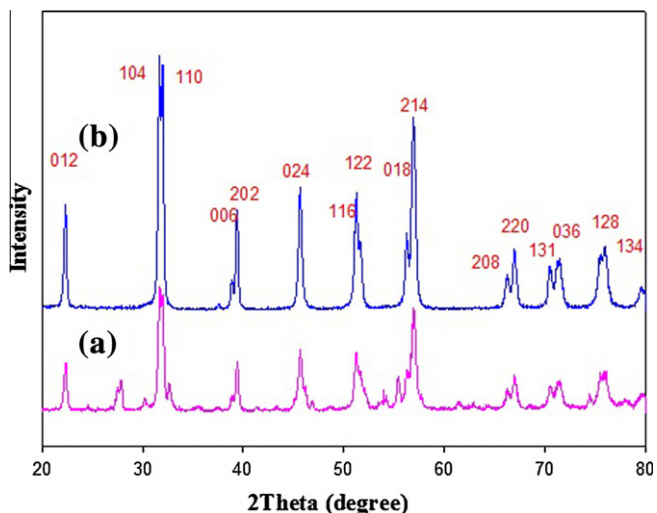


Fig. 1. XRD patterns of BFO nanoparticles synthesized by: (a) sol-gel, and (b) ultrasonic method.

and  $3500\text{ cm}^{-1}$  was attributed to O–H stretching, while a band around  $1622.45\text{ cm}^{-1}$  corresponds to the bending vibrations of  $\text{H}_2\text{O}$  [32]. The strong absorption peaks near  $440$  and  $559\text{ cm}^{-1}$  are assigned to Fe–O stretching and O–Fe–O bending vibrations of BFO nanoparticles, respectively, being characteristics of the octahedral  $\text{FeO}_6$  group in the perovskites compounds [33].

Fig. 1 shows the XRD patterns of BFO nanoparticles synthesized via ultrasound and sol-gel methods. In Fig. 1a, the impurity of  $\text{Bi}_2\text{O}_3$  was detected in the sample synthesized via sol-gel method but, under the similar conditions, pure BFO nanocrystals were synthesized via ultrasound (Fig. 1b). The reflection peaks of the sample prepared via ultrasound can be indexed as a single-phase perovskite structure belonging to the space group  $R3c$ , which is in good agreement with the literature data of JCPDS Card No. 86-1518. The calculated lattice parameters ( $a = b = 5.5774\text{ \AA}$  and  $c = 13.8667\text{ \AA}$ ) are in agreement with rhombohedral BFO nanoparticles according to the reported data. It can be seen from Fig. 1b that the diffraction peaks become broader for BFO nanoparticles prepared via ultrasound which is due to the smaller size of the particles. The average crystallite size obtained from the Debye–Scherrer formula was  $37.12\text{ nm}$  and  $81.43\text{ nm}$  for the samples prepared via ultrasound and sol-gel methods, respectively.

The smaller crystallite size of BFO nanoparticles prepared by ultrasound could be attributed to the higher rate of crystal nucleation than crystal growth during the sonication process [34].

The morphology of BFO samples were investigated by SEM, and TEM. Fig. 2a shows uniform nanoparticles with narrow size distribution. The mean particle size of the spherical nanoparticles is about  $60\text{--}80\text{ nm}$  based on Fig. 2b.

The magnetic properties of the as-synthesized BFO nanoparticles were measured by VSM at room temperature. Fig. 3 shows the variation of magnetization ( $M$ ) versus applied field ( $H$ ). As it is shown in Fig. 3, a weak FM order with a low magnetic saturation of about  $3.0\text{ emu g}^{-1}$  is observed for the BFO nanoparticles at  $300\text{ K}$ .

The TGA-DTA curves for BFO nanoparticles are shown in Fig. S4 from  $600$  to  $900\text{ }^\circ\text{C}$ . The weight of the sample remains constant over the whole temperature range. A distinct endothermic peak at around  $834\text{ }^\circ\text{C}$  (Curie temperature,  $T_c$ ) was observed which is attributed to the ferroelectric–paraelectric phase transition. The Curie temperature of BFO nanoparticles depending on the processing conditions that could vary slightly, and there is no agreement on the values of the Curie point for BFO by various research groups [35,36].

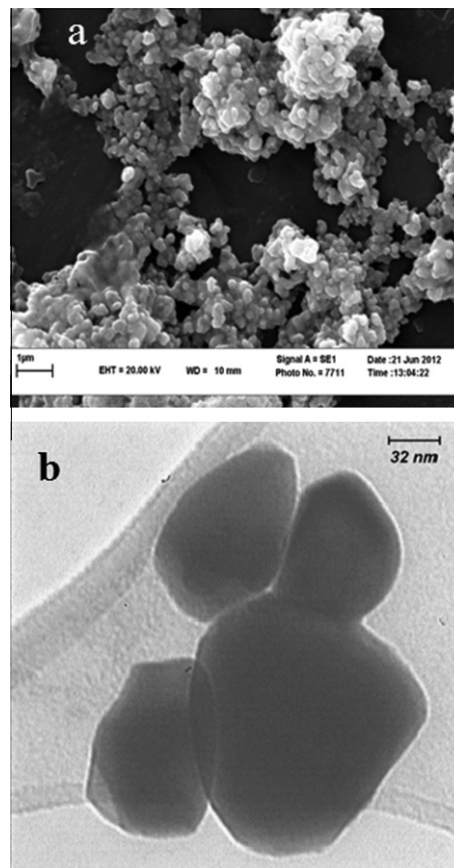


Fig. 2. (a) SEM, and (b) TEM images of the as-prepared BFO sample by ultrasound.

### 3.2. UV–vis DRS analysis

The optical absorption of the as-prepared BFO nanoparticles is important due to the UV–vis absorption edge which is related to the band gap energy of the photocatalyst. According to the UV–vis DRS spectrum (Fig. 4), the BFO nanoparticles have a strong photoabsorption property in the visible light region. As shown in the inset of Fig. 4, the band-gap energy was calculated by using Tauc's equation [37]. The corresponding band gap energy estimated by extrapolating the linear portion of  $(\alpha h\nu)^2$  against  $h\nu$  plot to the point  $a = 0$ . The band gap is estimated about  $2.00\text{ eV}$ , which is comparable with previous results  $2.10\text{ eV}$  and  $2.03\text{ eV}$  [38,39]. Thus, BFO nanoparticles may have a potential application as an appropriate photocatalyst for decomposition of materials in the visible region.

### 3.3. Removal of RhB

For comparison, the same photocatalytic degradation experiments were performed with BFO nanoparticles synthesized by sol-gel and ultrasonic methods. Although BFO nanoparticles synthesized in stricter conditions in sol-gel than ultrasonic method, but the sample synthesized with ultrasound exhibited a higher photoactivity (Fig. S5). During the acoustic cavitation process, very high temperatures ( $>5000\text{ K}$ ), pressures ( $>20\text{ MPa}$ ), and cooling rates ( $>10^{10}\text{ K s}^{-1}$ ) can be achieved upon the collapse of the bubbles [20,21,40] which provide a favorable environment for the anisotropic growth of the nanocrystals. Therefore, it is believed that ultrasound causes a higher surface area and smaller particle size of the products [41,42]. Under ultrasound the photocatalytic reaction area is increased and the efficiency of the electron–hole

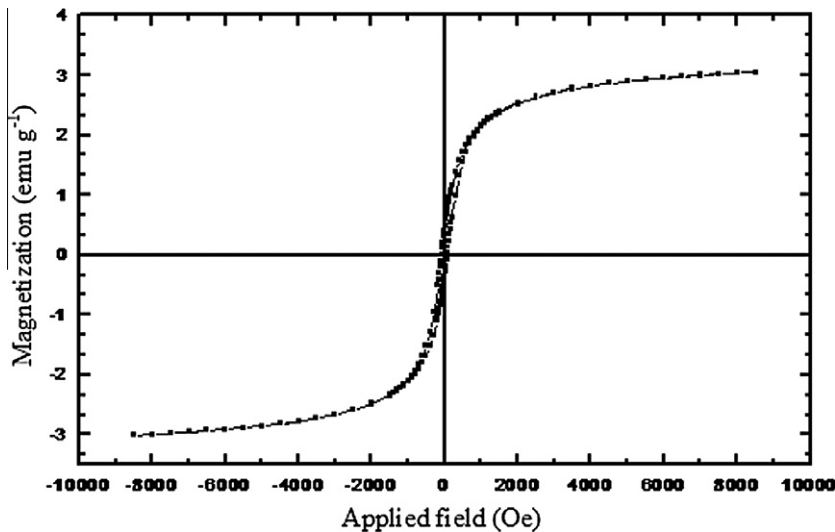


Fig. 3. Room temperature M–H hysteresis loop of BFO nanoparticles.

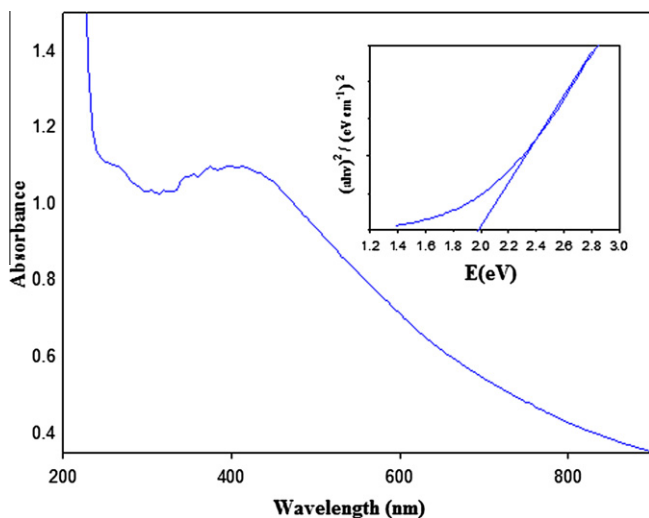


Fig. 4. UV–vis DRS spectrum of BFO, the inset shows the calculation of the band gap of BFO nanoparticles.

separation is also promoted [43,44]. As the results showed that the sample synthesized via ultrasound exhibited higher photocatalytic activity than the sample synthesized via sol–gel method, therefore, the whole experiments were performed with the sample prepared by ultrasound.

#### 3.4. The pH of medium

The effect of pH on the photodegradation efficiency of the dye is very important, because it influences the surface-charge-properties of the photocatalyst and affects the ionic species in the solution. Hence, the adsorption of dye molecules changes onto the photocatalyst surfaces at different pH. As shown in Fig. 5, in natural pH of the solution (4.3) and in basic medium (pH = 10.0), the photodegradation rate of RhB over BFO nanoparticles surface can be ignored. But with decreasing the pH from 4.3 to 3.5, the photodegradation rate of RhB greatly increased. However, a drastic increase of the photodegradation rate was found at pH 2.5.

The charge state of RhB is dependent to the pH of solution. The  $pK_a$  value for the aromatic carboxyl group presented on the RhB molecule is about 4.0. When the pH of solution is lower than 4.0, the carboxylic groups on the RhB are shifted to acidic form. Due

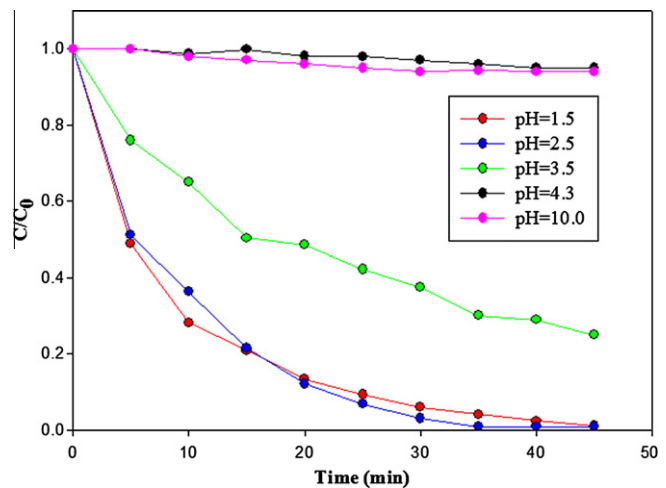


Fig. 5. Photocatalytic degradation of RhB on BFO nanoparticles at different pH.

to the equilibrium, there are some available carboxylic anions in the solution that adsorbed on the surface and then the equilibrium shifted to compensate the adsorbed species. This process can be continued until a complete removal (Fig. S6a).

When the pH of solution is higher than 4.0, the carboxylic acid group can be ionized and the zwitterion form of RhB (Fig. S6b) is formed [45]. In addition, the zwitterion form of RhB in water may increase dimerization of RhB due to the attractive electrostatic interactions between the carboxyl and xanthenes groups of the monomers. This makes the molecule too large and the density of the charges is reduced due to the mutual interactions between two monomers and under this condition the RhB removal might be inhibited [46,47].

On the other hand, at  $pH > pH_{PZC}$  ( $pH_{PZC} = 7$ ) of the BFO, excessive  $OH^-$  compete with  $COO^-$  in binding with  $-N^+$  and the aggregation of RhB decreases, so the solid surface is negatively charged and the BFO nanoparticles repels the  $COO^-$  groups on the RhB at basic condition. Therefore, the amount of adsorption and degradation were completely decreased on the surface of photocatalyst.

#### 3.5. Adsorption isotherm

The adsorption of organic molecules on the surface of catalyst plays an important role in the photocatalytic process. Therefore,

it is important to determine the adsorption isotherm. As the catalyst is active with respect to the light, the adsorption isotherm was carried out in the dark place. The Langmuir model was applied on the experimental data and the linear form of the Langmuir model is represented by the following equation [48]:

$$\frac{c_e}{q_e} = \left(\frac{1}{q_m K}\right) \left(\frac{1}{q_m}\right) c_e \quad (1)$$

where  $q_e$  ( $\text{mg g}^{-1}$ ) is the amount of dye adsorbed on the catalyst at equilibrium,  $c_{eq}$  ( $\text{mg L}^{-1}$ ) is the dye concentration in solution at the equilibrium,  $K$  ( $\text{L mg}^{-1}$ ) is the equilibrium constant, and  $q_{max}$  ( $\text{mg g}^{-1}$ ) is the maximum amount of dye adsorbed on the catalyst. The calculated values of the Langmuir parameters are  $K = 0.163 \text{ L mg}^{-1}$ ,  $0.115 \text{ L mg}^{-1}$  and  $q_{max} = 64.22 \text{ mg g}^{-1}$ ,  $55.42 \text{ mg g}^{-1}$  for the sample synthesized via ultrasound and sol-gel methods, respectively (Fig. S7). The BFO exhibited a high adsorption at dark that is appropriate for high photodegradation of dye on the surface of BFO.

### 3.6. Photocatalytic degradation

Before irradiation, the solution was magnetically stirred in the dark place for different interval times to attain adsorption-desorption equilibrium between the dye and photocatalyst. The optimum time to reach equilibrium was 10 min. Then the solution, after reaching equilibrium in the dark, was placed in the presence of sunlight irradiation for different interval times and the UV-vis absorption results was shown in Fig. 6a. According to Fig. 6a, the absorption peak decreases considerably throughout the irradiation time and shifts to lower wavelengths based on the N-de-ethylation

mechanism [49]. Inset of Fig. 6a shows a shift of 31 nm for the solution under sunlight irradiation in 20 min.

After 30 min irradiation, a fully N-de-ethylation and break up conjugated xanthene ring take place under sunlight conditions. Fig. 6b shows the color change of RhB solution during the sunlight irradiation.

Desorption of species from the surface of the catalyst (in dark and light) was performed and the concentration of RhB in the solution and on the surface are shown in Fig. 6d. After reaching equilibrium in dark, according to the desorption test from the adsorbed sample, approximately 63% of RhB was adsorbed and the rest was remained in the solution. This result shows that the BFO nanoparticles have a high adsorption capacity for RhB that is favor for the photocatalytic decomposition. The FT-IR (Fig. S8) result confirmed the adsorption of RhB on the surface of BFO nanoparticles in the dark place.

In the presence of sunlight irradiation, the concentration of RhB was decreased on the surface and replaced by the solution. After 30 min of sunlight irradiation, the concentration of RhB in solution was zero, but some dyes (10%) remained on the surface of the photocatalyst that needs more time for complete degradation (Fig. 6d). After 35 min of irradiation, the RhB remained on the surface of BFO nanoparticles was degraded too.

It is also demonstrated that the color of the catalyst before and after use was the same. It means that RhB is degraded completely because there is no RhB in the solution and on the catalyst (Fig. 6c). In addition, the FT-IR results in Fig. S8 confirmed this claim.

Besides the removal of color, the lowering of TOC was another important parameter in degradation process. Fig. 6e shows the TOC changes of RhB solution during the sunlight irradiation. In

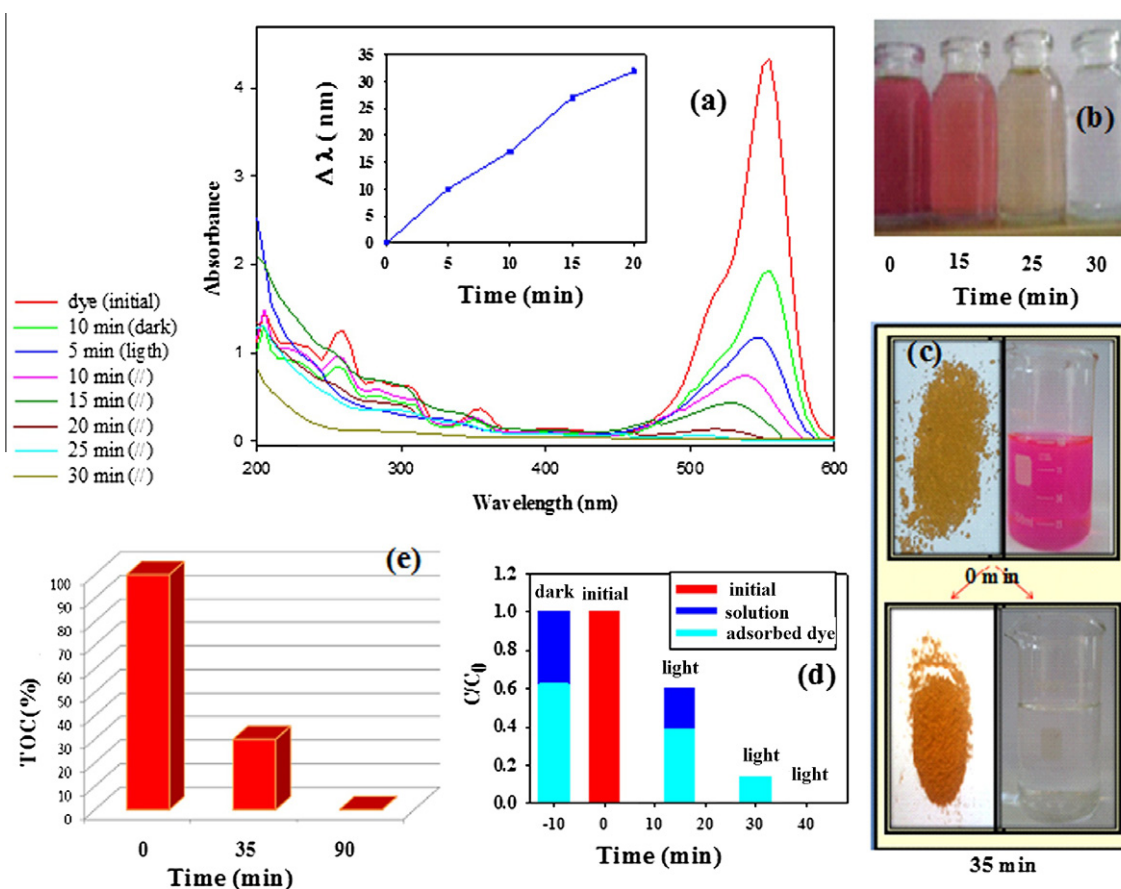


**Fig. 6.** (a) UV-vis absorption spectra of RhB solution at different contact times with BFO nanoparticles, the inset is the change of wavelength with time, (b) The color change of RhB during the process, (c) comparison of initial and final states of the process, (d) the remaining concentration of RhB in solution and on the surface of BFO during the irradiation, and (e) TOC change of RhB solution versus time.

35 min of irradiation, 70% of TOC was decreased and with increasing the time of irradiation to 90 min, the total organic species were removed from the solution.

Some other experiments were carried out without pre-equilibrium in dark and the catalyst was directly mixed with the RhB solution under the sunlight in different interval times. The results were similar with and without pre-equilibrium conditions (Fig. S9). After 40 min of sunlight irradiation a complete degradation was appeared (not shown).

### 3.7. Kinetics of photocatalytic degradation

Different initial concentrations of RhB ( $15 \text{ mg L}^{-1}$ ,  $25 \text{ mg L}^{-1}$ ,  $50 \text{ mg L}^{-1}$ ,  $75 \text{ mg L}^{-1}$ ) were used for the photocatalytic kinetics of BFO nanoparticles synthesized in two different methods as shown in Fig. 7. To calculate the rate constant of photocatalytic degradation, Langmuir–Hinshelwood model based on Eq. (2) was applied.

$$r = -\frac{dc}{dt} = \frac{k_r K_c}{1 + K_c} \quad (2)$$

In this equation,  $r$  ( $\text{mg L}^{-1} \text{ min}^{-1}$ ),  $k_r$  ( $\text{mg L}^{-1} \text{ min}^{-1}$ ),  $K$  ( $\text{L mg}^{-1}$ ),  $c$  ( $\text{mg L}^{-1}$ ) and  $t$  (min) are the reaction rate, reaction rate constant, adsorption coefficient of the reactant, reactant concentration and time of illumination, respectively. When  $c$  is very small, Eq. (2) can be converted to following equation:

$$r = -\frac{dc}{dt} = k_r K_c = kc \quad (3)$$

where  $k$  ( $\text{min}^{-1}$ ) is the first-order rate constant.

With setting  $t = 0$ ,  $c = c_0$ , Eq. (3) can be expressed by the following equation:

$$\ln \frac{c}{c_0} = -Kt \quad (4)$$

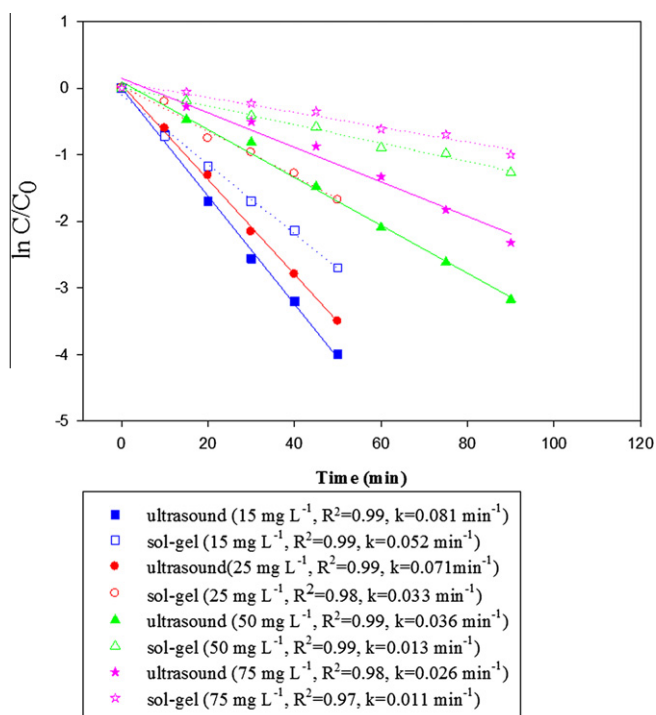


Fig. 7. Photocatalytic kinetics of BFO with different initial concentrations of RhB. (Solid line and dotted line are samples synthesized via ultrasound and sol-gel, respectively.)

In this equation  $c_0$  is the initial concentration and  $c$  is the summation of surface and solution concentrations of RhB at each time. The surface concentration was measured by desorption process. The photocatalytic degradation is apparent first-order kinetics based on the Langmuir–Hinshelwood model, and the rate constants were determined by assuming pseudo-first-order reaction kinetics [50].

The plots of  $\ln \frac{c}{c_0}$  versus irradiation time ( $t$ ) exhibited a straight line, and via its slope could determine reaction rate constant of degradation (Fig. 7). It can be seen that the initial concentration of RhB has a significant effect on the degradation rates, as the rate constant of photodegradation of RhB is higher when the initial concentration is lower. This could be explained that the amount of active centers on the photocatalyst is finite, and the excessive molecules of RhB in the medium causes a reduction in the light adsorption capability of the catalyst. Thus, the photocatalytic process is influenced by the initial concentration of RhB. Also, at the same illumination time, the relative amount of RhB dye decomposed is higher for the sample synthesized with ultrasound than the sample synthesized with sol-gel method. This is related to the effect of ultrasound that explained before.

### 3.8. Stability and reusability of the catalyst

Estimating the stability and reusability of the catalyst is necessary for the evaluation of its practical applications. To investigate the reusability of BFO nanoparticles in the reaction, the photodegradation experiment was repeated five times. In each time, after using, BFO nanoparticles were separated from the solution with an external magnetic field. Then, the collected sample repeatedly used in successive cycles. In each cycle, BFO nanoparticles (0.05 g) were added to 100 mL dye ( $0.50 \text{ g L}^{-1}$  BFO). As displayed in Fig. 8, RhB was quickly decomposed in each cycle. This suggests that there is no significant loss of activity after four cycles and there is a little loss of activity in fifth cycle. It is also confirmed that the BFO nanoparticles was stable during the photocatalytic oxidation process. In addition, there was no difference between the FT-IR of the original sample and the samples in the successive cycles (Fig. S10).

### 3.9. Visible light driven degradation mechanism

Some experiments were designed to determine the mechanism of degradation. At first, one experiment was carried out in an aqueous RhB solution without BFO nanoparticles. The result showed

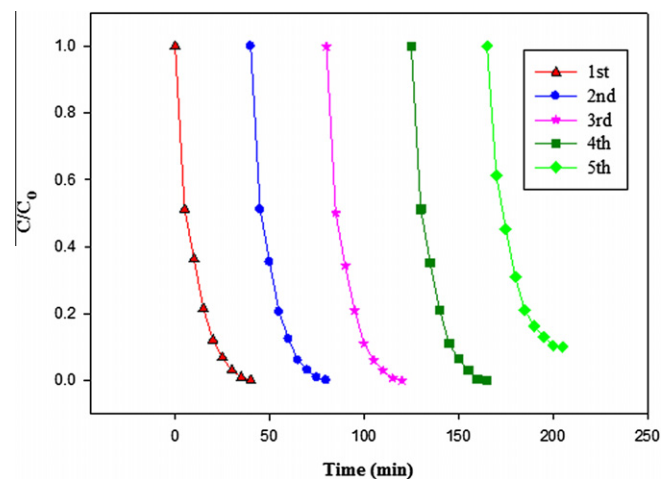


Fig. 8. Photocatalytic degradation of RhB in successive cycles on BFO nanoparticles.

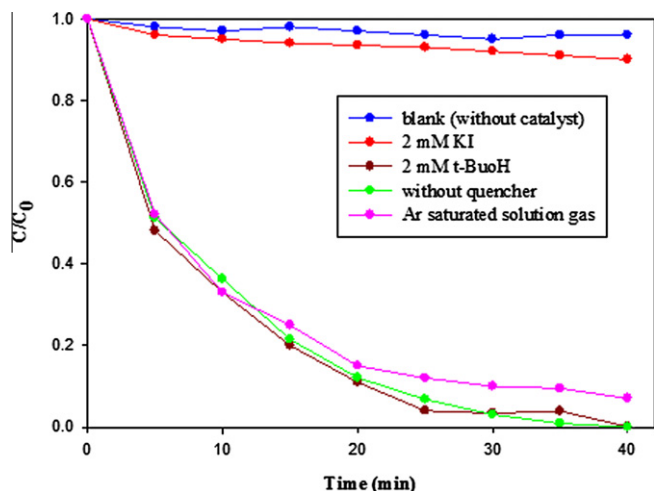


Fig. 9. Effect of different scavengers on the photocatalytic activity of BFO nanoparticles.

that the absorption intensity and the absorption wavelength did not change with increasing the irradiation time. It means that RhB was stable versus light irradiation without catalyst.

To further understanding the effect of active species, two separate experiments were performed in the presence and absence of quenchers in the solution, under identical conditions.

As it is shown in Fig. 9, after addition of KI (a quencher of positive hole and  $\text{HO}^\cdot$  radicals on the catalyst surface with redox potential of 1.3 V for the couple  $\text{I}^\cdot/\text{I}^-$ ) [51], the degradation rate of RhB was strongly inhibited. This result suggests that the degradation of RhB were mainly done by the hole and/or  $\cdot\text{OH}_{\text{ads}}$ . For identification the role of each of them (hole and  $\text{OH}^\cdot$ ), t-butyl alcohol as a scavenger of  $\text{OH}^\cdot$  was added to the solution. Based on Fig. 9, by addition of t-butyl alcohol, the rate of degradation was not changed. This implies that hydroxyl radicals do not play a major role in the degradation of the RhB. This behavior could be attributed to the position of valance band potentials of BFO at the point of zero charge ( $\text{pH}_{\text{PZC}}$ ) that can be calculated by empirical equation [52–54].

Based on empirical equation, the valance band potential ( $V_{\text{VB}}$ ) of BFO nanoparticles is about 2.535 V which is lower than the standard redox potential of  $\text{OH}^\cdot$ ,  $\text{H}^+/\text{H}_2\text{O}$  (2.7 V versus NHE) [55] as shown in Fig. 10. In another word, the photogenerated hole cannot oxidize the  $\text{H}_2\text{O}$  to form  $\text{OH}^\cdot$ .

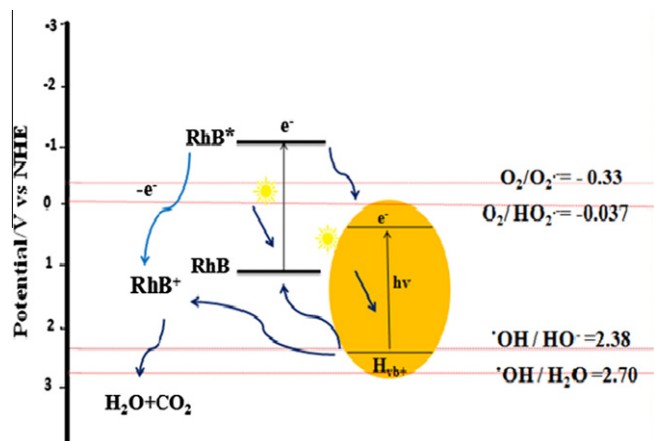


Fig. 10. Scheme diagram of the photocatalytic reaction of RhB on BFO nanoparticles.

Furthermore, RhB can absorb visible light in the range of 460–600 nm which is attributed to its ground and the excited states [53]. The relative positions of the standard redox potential of the  $\text{RhB}^\cdot/\text{RhB}^+$  is about  $-1.09$  V s. NHE, and  $\text{RhB}/\text{RhB}^+$  is about 1.46 V versus NHE [56]. Under sunlight irradiation, some electrons can transfer from excited state of adsorbed dye to the conduction band (CB) of BFO nanoparticles. The transferred electrons can be trapped by some species on the surface.

One experiment was also conducted to understand the effect of oxygen. As shown in Fig. 9, the photodegradation efficiency of RhB was decreased slightly under Ar atmosphere which means that  $\text{O}_2$  has a negligible effect in degradation. This behavior may be attributed to the conduction band potential ( $V_{\text{CB}}$ ) position of BFO nanoparticles and  $\text{O}_2/\text{O}_2^{\cdot-}$  (Fig. 10).

### 3.10. Identification of intermediates

#### 3.10.1. FT-IR analysis

The process of degradation of RhB was further examined with FT-IR (Fig. S11). According to the literature, the assignments for the RhB (before irradiation) exhibited several bands [57,58]. After 35 min of irradiation, nearly the vibrations of the carbon–nitrogen bond, the C–aryl bond, and all of the aromatic skeletal and heterocyclic vibrations were disappeared. The band vibrations due to methyl groups at  $1476$  and  $1446$   $\text{cm}^{-1}$  are shifted to  $1465$   $\text{cm}^{-1}$  and several new peaks are produced. The new strong absorption at  $1022$ – $1097$   $\text{cm}^{-1}$  may be related to  $-\text{C}-\text{O}-\text{H}$  stretch vibration. The strong absorption in the region  $2854$ – $2959$   $\text{cm}^{-1}$  suggests the intermediates containing  $-\text{CH}_2-$  and  $\text{C}-\text{CH}_3$ . In overall, the FT-IR results show that the large conjugated chromospheres structure of the dye was destroyed and smaller organic molecules were formed under solar light irradiation.

#### 3.10.2. GC–MS spectrum

In order to describe the photodegradation pathways and detect the intermediates during the photodegradation, the GC–MS analysis was used. Fig. 11 shows the GC chromatogram and Table S1 shows the identified intermediates for the sample degraded under direct sunlight irradiation in 35 min. The results of UV–vis show that the N–de-ethylation of RhB takes place completely. In the sunlight irradiations, the intermediates contain benzene rings were produced in initial stages of destruction of the conjugated chromophoric structure of the dye. The relative intensities were decreased considerably in further degradation and led to the colorless

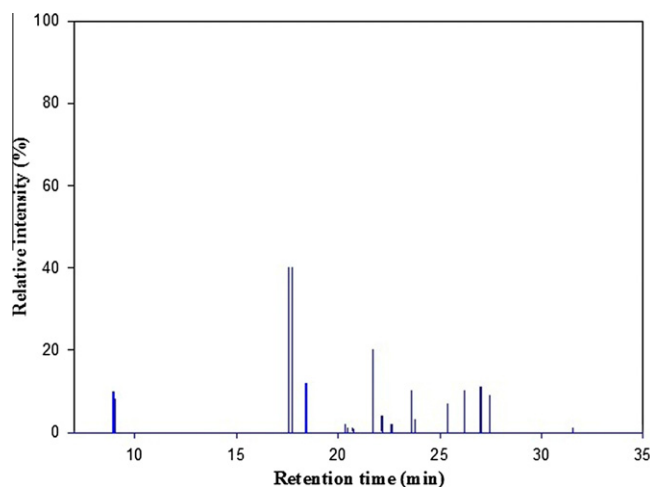


Fig. 11. GC chromatogram of the intermediates obtained from the photocatalytic degradation of RhB on BFO nanoparticles.

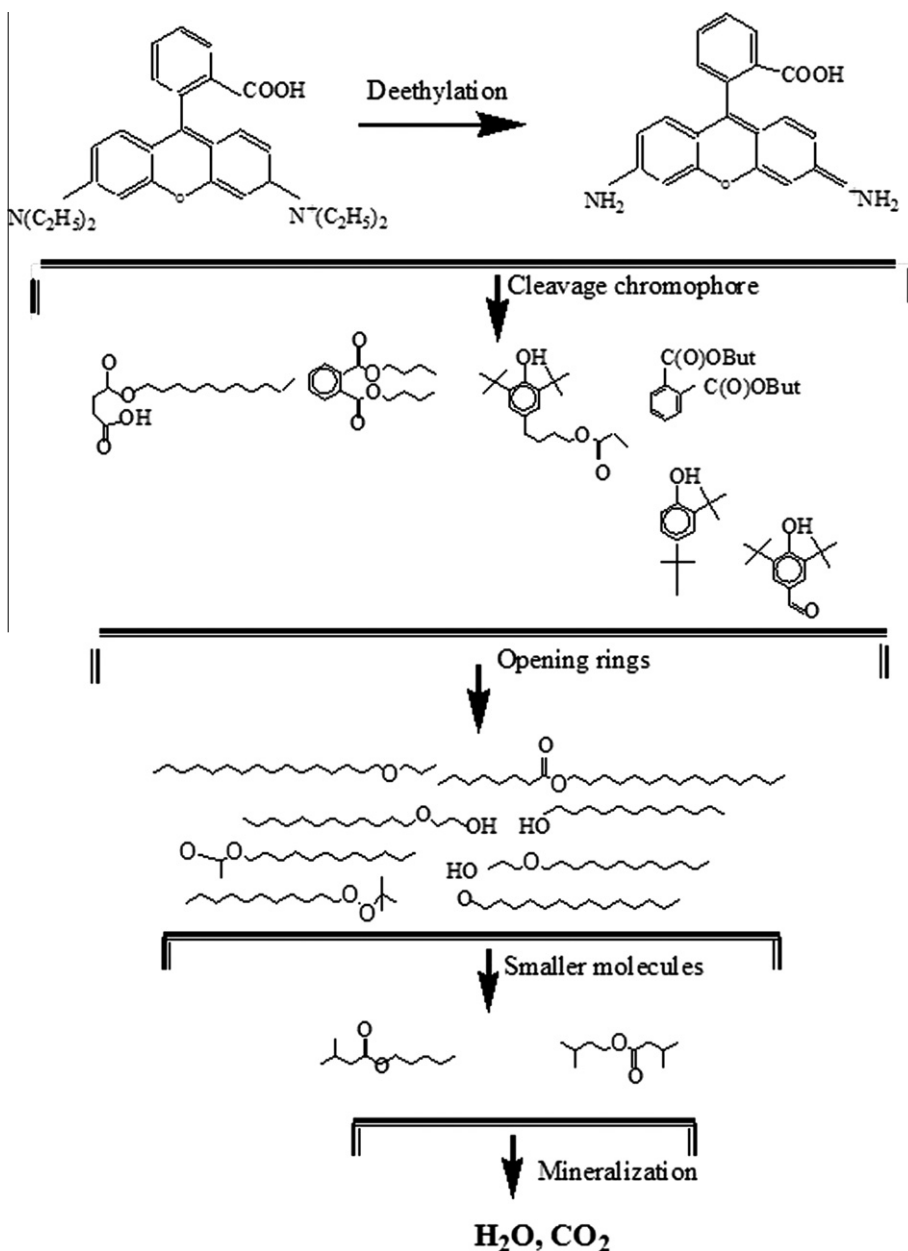


Fig. 12. Proposed mechanism of the photocatalytic degradation of RhB on BFO nanoparticles.

compounds and finally most of them convert to  $CO_2$  and  $H_2O$  at the end of the process (35 min). In this system, the major products are corresponding to peaks ( $t_r = 17.558$  min), ( $t_r = 17.758$  min), ( $t_r = 18.075$  min), ( $t_r = 21.717$  min) and ( $t_r = 22.508$  min), respectively as shown in Fig. 11. The structure, formula, intensity and retention times of the products are presented in the Table S1. It is very important to mention that by increasing the time of irradiation to 90 min, a complete mineralization was achieved.

### 3.11. Photocatalytic degradation pathway of RhB

UV-vis analysis shows that, under direct sunlight irradiation, two competitive processes occurred during the photocatalytic reactions: N-deethylation and destruction of the dye chromophores. Fully N-de-ethylation and the destruction of the conjugated structure were confirmed by FT-IR and GC-mass after 35 min. According to the GC-mass results, the photocatalytic deg-

radation of RhB can be preceded by cleavage of the central carbon atom to generate benzene rings, opening of benzene rings to produce small molecular compounds. According to the TOC results, approximately 70% of the total organic carbon reduced in 35 min, and the remaining were some small organic molecules that detected with GC-mass analysis. Finally, the mineralization of the intermediates can be completed in 90 min. Fig. 12 shows the proposed mechanism for the degradation of RhB under sunlight irradiation.

## 4. Conclusions

In this work, pure BFO nanoparticles were prepared successfully by ultrasound without any additives in short time and low temperature. The BFO nanoparticles with measured band gap of 2.0 eV exhibited high crystallization, smaller crystallite size in comparison with the sample prepared by sol-gel method. The synthesized

catalyst showed a weak FM order at room temperature and a Curie temperature at 834 °C ( $T_C$ ) which is attributed to the ferroelectric-to-paraelectric phase transition. The results show that, the conjugated chromophore structure of RhB was completely destroyed under direct sunlight irradiation in 35 min. The total organic carbon measurement displayed a complete mineralization after 90 min of irradiation. The photocatalyst was stable and active under visible light irradiation after four successive cycle uses. The photocatalytic degradation of RhB on BFO nanoparticles could be preceded via direct reactions of RhB with holes trapped on the surface. In addition, the photocatalytic degradation of RhB by BFO nanoparticles were apparent first-order kinetics based on the Langmuir–Hinshelwood model.

### Acknowledgement

The support of Ferdowsi University of Mashhad (Research and Technology) for this work (code 3/19022, date 2011/10/19) is appreciated.

### Appendix A. Supplementary material

Supplementary data associated with this article can be found, in the online version, at <http://dx.doi.org/10.1016/j.cej.2013.02.124>.

### References

- [1] P. Borker, A.V. Salker, Photocatalytic degradation of textile azo dye over  $Ce_{1-x}Sn_xO_2$  series, *Mater. Sci. Eng. B* 133 (2006) 55–60.
- [2] W.W. Leeb, W.H. Chung, C.S. Lud, W.Y. Linc, C.C. Chen, A study on the degradation efficiency and mechanisms of ethyl violet by HPLC–PDA–ESI–MS and GC–MS, *Sep. Purif. Technol.* 98 (2012) 488–496.
- [3] W.L.W. Lee, S.T. Huang, J.L. Chang, J.Y. Chen, M.C. Cheng, C.C. Chen, Photodegradation of CV over nanocrystalline bismuth tungstate prepared by hydrothermal synthesis, *J. Mol. Catal. A: Chem.* 361–362 (2012) 80–90.
- [4] Y.H.B. Liao, J.X. Wang, J.S. Lin, W.H. Chung, W.Y. Lin, C.C. Chen, Synthesis, photocatalytic activities and degradation mechanism of  $Bi_2WO_6$  toward crystal violet dye, *Catal. Today* 174 (2011) 148–159.
- [5] M.A. Brown, S.C. De-Vito, Predicting azo dye toxicity, *Crit. Rev. Environ. Sci. Technol.* 23 (1993) 249–324.
- [6] I.K. Konstantinou, T.A. Albanis,  $TiO_2$ -assisted photocatalytic degradation of azo dyes in aqueous solution: kinetic and mechanistic investigations, *Appl. Catal. B: Environ.* 49 (2004) 1–14.
- [7] D. Zhao, C.C. Chen, Y. Wang, W.H. Ma, J.C. Zhao, T. Rajh, L. Zang, Enhanced photocatalytic degradation of dye pollutants under visible irradiation on Al (III)-modified  $TiO_2$ : structure, interaction, and interfacial electron transfer, *Environ. Sci. Technol.* 42 (2008) 308–314.
- [8] K. Nagaveni, M.S. Hegde, G. Madras, Structure and photocatalytic activity of  $Ti_{1-x}M_xO_{2+d}$  ( $M = W, V, Ce, Zr, Fe$  and  $Cu$ ) synthesized by solution combustion method, *J. Phys. Chem. B* 108 (2004) 20204–20212.
- [9] A. Fujishima, T.N. Rao, D.A. Tryk, Titanium dioxide photocatalysis, *J. Photochem. Photobiol. C* 1 (2000) 1–21.
- [10] S.V. Kalinin, M.R. Suichomel, P.K. Davies, D.A. Bonnel, Potential and impedance imaging of polycrystalline  $BiFeO_3$  Ceramics, *J. Am. Ceram. Soc.* 85 (2002) 3011–3017.
- [11] Y.G. Wang, G. Xu, Z.H. Ren, X. Wei, W.J. Weng, P. Du, G. Shen, G.R. Han, Mineralizer-assisted hydrothermal synthesis and characterization of  $BiFeO_3$  nanoparticles, *J. Am. Ceram. Soc.* 90 (2007) 2615–2617.
- [12] T. Choi, S. Lee, Y.J. Choi, V. Kiryukhin, S.W. Cheong, Switchable ferroelectric diode and photovoltaic effect in  $BiFeO_3$ , *Science* 324 (2009) 63–66.
- [13] F. Gao, X.Y. Chen, K.B. Yin, S. Dong, Z.F. Ren, F. Yuan, T. Yu, Z.G. Zou, J.M. Liu, Visible-light photocatalytic properties of weak magnetic  $BiFeO_3$  nanoparticles, *Adv. Mater.* 19 (2007) 2889–2892.
- [14] W. Luo, L. Zhu, N. Wang, H. Tang, M. Cao, Y. She, Efficient removal of organic pollutants with magnetic nanoscaled  $BiFeO_3$  as a reusable heterogeneous Fenton-like catalyst, *Environ. Sci. Technol.* 44 (2010) 1786–1791.
- [15] F. Gao, Y. Yuan, K.F. Wang, X.Y. Chen, F. Chen, J.-M. Liu, Z.F. Ren, Preparation and photoabsorption characterization of  $BiFeO_3$  nanowires, *Appl. Phys. Lett.* 89 (2006) 102506–102508.
- [16] J. Luo, P.A. Maggard, Hydrothermal synthesis and photocatalytic activities of  $SrTiO_3$ -coated  $Fe_2O_3$  and  $BiFeO_3$ , *Adv. Mater.* 18 (2006) 514–517.
- [17] S. Farhadi, M. Zaidi, Bismuth ferrite ( $BiFeO_3$ ) nanopowder prepared by sucrose-assisted combustion method, *J. Mol. Catal. A: Chem.* 299 (2009) 18–25.
- [18] G.D. Achenbach, W.J. James, R. Gerson, Preparation of single-phase polycrystalline  $BiFeO_3$ , *J. Am. Ceram. Soc.* 8 (1967) 437–438.
- [19] S. Shetty, V.R. Palkar, R. Pinto, Size effect study in magnetoelectric  $BiFeO_3$  system, *Pramana: J. Phys.* 58 (2002) 1027–1030.
- [20] L. Zhou, W. Wang, S. Liu, L. Zhang, H. Xu, W. Zhu, A sonochemical route to visible-light-driven high-activity  $BiVO_4$  photocatalyst, *J. Mol. Catal. A* 252 (2006) 120–124.
- [21] N.A. Dhas, K.S. Suslick, Sonochemical preparation of hollow nanospheres and hollow nanocrystals, *J. Am. Chem. Soc.* 127 (2005) 2368–2369.
- [22] M.H. Entezari, N. Ghows, Micro-emulsion under ultrasound facilitates the fast synthesis of quantum dots of CdS at low temperature, *Ultrason. Sonochem.* 18 (2011) 127–134.
- [23] N. Ghows, M.H. Entezari, Ultrasound with low intensity assisted the synthesis of nanocrystalline  $TiO_2$  without calcinations, *Ultrason. Sonochem.* 17 (2010) 878–883.
- [24] N. Ghows, M.H. Entezari, A novel method for the synthesis of CdS nanoparticles without surfactant, *Ultrason. Sonochem.* 18 (2011) 269–275.
- [25] N. Ghows, M.H. Entezari, Fast and easy synthesis of core-shell nanocrystal ( $CdS/TiO_2$ ) at low temperature by micro-emulsion under ultrasound, *Ultrason. Sonochem.* 18 (2011) 629–634.
- [26] M.H. Entezari, Z. Sharif Al-Hoseini, Sono-sorption as a new method for the removal of methylene blue from aqueous solution, *Ultrason. Sonochem.* 14 (2007) 599–604.
- [27] M.H. Entezari, Z. Sharif Al-Hoseini, N. Ashraf, Fast and efficient removal of Reactive Black 5 from aqueous solution by a combined method of ultrasound and sorption process, *Ultrason. Sonochem.* 15 (2008) 433–437.
- [28] N. Ghows, M.H. Entezari, Exceptional catalytic efficiency in mineralization of the reactive textile azo dye (RB5) by a combination of ultrasound and core shell nanoparticles ( $CdS/TiO_2$ ), *J. Hazard. Mater.* 195 (2011) 132–138.
- [29] N. Ghows, M.H. Entezari, Kinetic investigation on sono-degradation of Reactive Black 5 with core-shell nanocrystal, *Ultrason. Sonochem.* 20 (2013) 386–394.
- [30] S.M. Nomanbhai, K. Palanisamy, Removal of heavy metal from industrial wastewater using chitosan coated oil palm shell charcoal, *Electron. J. Biotechnol.* 8 (2005) 43–53.
- [31] S. Ahmed, M.G. Rasul, R. Brown, M.A. Hashib, Influence of parameters on the heterogeneous photocatalytic degradation of pesticides and phenolic contaminants in wastewater, *J. Environ. Manage.* 92 (2011) 311–330.
- [32] S.H. Han, K.S. Kim, H.G. Kim, H.G. Lee, H.W. Kang, J.S. Kim, C.I. Cheon, Synthesis and characterization of multiferroic  $BiFeO_3$  powders fabricated by hydrothermal method, *Ceram. Int.* 36 (2010) 1365–1372.
- [33] G.V. Subba Rao, C.N.R. Rao, Infrared and electronic spectra of rare earth perovskites: ortho-chromites, -manganites and -ferrites, *Appl. Spectrosc.* 24 (1970) 436–445.
- [34] M. Yoon, M. Seo, C. Jeong, J.H. Jang, K.S. Jeon, Synthesis of liposome-templated titania nanodisks: optical properties and photocatalytic activities, *Chem. Mater.* 17 (2005) 6069–6079.
- [35] V. Fruth, L. Mitoseriu, D. Berger, A. Ianculescu, C. Matei, S. Preda, M. Zaharescu, Preparation and characterization of  $BiFeO_3$  ceramics, *Prog. Solid State Chem.* 35 (2007) 193–202.
- [36] X. Wang, Y. Zhang, Z. Wu, Magnetic and optical properties of multiferroic bismuth ferrite nanoparticles by tartaric acid-assisted sol-gel strategy, *Mater. Lett.* 64 (2010) 486–488.
- [37] D.A. Chang, P. Lin, T.Y. Tseng, Optical properties of  $ZrTiO_4$  films grown by radio-frequency magnetron sputtering, *J. Appl. Phys.* 77 (1995) 4445–4451.
- [38] Y.N. Huo, Y. Jin, Y. Zhang, Citric acid assisted solvothermal synthesis of  $BiFeO_3$  microspheres with high visible-light photocatalytic activity, *J. Mol. Catal. A: Chem.* 331 (2010) 15–20.
- [39] R.Q. Guo, L. Fang, W. Dong, F. Zheng, M. Shen, Enhanced photocatalytic activity and ferromagnetism in Gd doped  $BiFeO_3$  nanoparticles, *J. Phys. Chem. C* 114 (2010) 21390–21396.
- [40] K.S. Suslick, S.B. Choe, A.A. Cichowlas, M.W. Grinstaff, Sonochemical synthesis of amorphous Iron, *Nature* 353 (1991) 414–416.
- [41] L. Zhou, W. Wang, L. Zhang, Ultrasonic-assisted synthesis of visible-light-induced  $Bi_2MO_6$  ( $M = W, Mo$ ) photocatalysts, *J. Mol. Catal. A: Chem.* 268 (2007) 195–200.
- [42] J. Lishan, D. Tong, L. Qingbiao, T. Yong, Study of photocatalytic performance of  $SrFeO_{3-x}$  by ultrasonic radiation, *Catal. Commun.* 8 (2007) 963–966.
- [43] D. Wang, J. Tang, Z. Zou, J. Ye, Photophysical and photocatalytic properties of a new series of visible-light-driven photocatalysts  $M_3V_2O_8$  ( $M = Mg, Ni, Zn$ ), *Chem. Mater.* 17 (2005) 5177–5182.
- [44] J.G. Yu, J.F. Xiong, B. Cheng, S.W. Liu, Fabrication and characterization of  $Ag-TiO_2$  multiphase nanocomposite thin films with enhanced photocatalytic activity, *Appl. Catal. B* 60 (2005) 211–221.
- [45] A.V. Deshpande, U. Kumar, Effect of method of preparation on photophysical properties of RhB impregnated sol-gel hosts, *J. Non-Cryst. Solids* 306 (2002) 149–159.
- [46] A. Ghanadzadeh, M.A. Zanjanchi, R. Tirbandpay, The role of host environment on the aggregative properties of some ionic dye materials, *J. Mol. Struct.* 616 (2002) 167–174.
- [47] I. Lopez Arbeloa, P. Ruiz Ojeda, Dimeric states of Rhodamine B, *Chem. Phys. Lett.* 87 (1982) 556–560.
- [48] N. Takeda, T. Torimoto, S. Sampath, S. Kuwabata, H. Yoneyama, Effect of inert supports for titanium dioxide loading on enhancement of photodecomposition rate of gaseous propionaldehyde, *J. Phys. Chem.* 99 (1995) 9986–9991.
- [49] S. Horikoshi, A. Saitou, H. Hidaka, N. Serpone, Thermal/non-thermal effects of microwave irradiation on the mechanism of the photocatalyzed degradation of rhodamine-B dye under UV/vis irradiation, *Environ. Sci. Technol.* 37 (2003) 5813–5822.

- [50] J. Xu, W. Wang, M. Shang, S. Sun, J. Ren, L. Zhang, Efficient visible light induced degradation of organic contaminants by  $\text{Bi}_2\text{WO}_6$  film on  $\text{SiO}_2$  modified reticular substrate, *Appl. Catal. B: Environ.* 93 (2010) 227–232.
- [51] G.T. Li, J.H. Qu, X.W. Zhang, J.H. Liu, H.N. Liu, Electrochemically assisted photocatalytic degradation of Orange II: influence of initial pH values, *J. Mol. Catal. A: Chem.* 259 (2006) 238–244.
- [52] A.H. Nethercot, Prediction of fermi energies and photoelectric threshold based on electronegativity concepts, *Phys. Rev. Lett.* 33 (1974) 1088–1091.
- [53] F. Hongbo, P. Chengshi, Y. Wenqing, Z. Yongfa, Visible-light-induced degradation of Rhodamine B by nanosized  $\text{Bi}_2\text{WO}_6$ , *J. Phys. Chem. B.* 109 (2005) 22432–22439.
- [54] Y.I. Kim, S.J. Atherton, E.S. Brigham, T.E. Mallouk, Sensitized layered metal oxide semiconductor particles for photochemical hydrogen evolution from nonsacrificial electron donors, *J. Phys. Chem.* 97 (1993) 11802–11810.
- [55] A.J. Bard, R. Parsons, J. Jordan, *Standard Potentials in Aqueous Solution*, Marcel Dekker, New York, 1985.
- [56] T. Watanabe, T. Takizawa, K. Honda, Photocatalysis through excitation of adsorbates. I, highly efficient N-deethylation of rhodamine, *J. Phys. Chem.* 81 (1977) 1845–1851.
- [57] G.M. Liu, C.J. Zhao, Photocatalytic degradation of dye sulforhodamine B: a comparative study of photocatalysis with photosensitization, *New J. Chem.* 24 (2000) 411–417.
- [58] G.M. Liu, C.J. Zhao, Photooxidation pathway of sulforhodamine-B: dependence on the adsorption mode on  $\text{TiO}_2$  exposed to visible light radiation, *Environ. Sci. Technol.* 34 (2000) 3982–3990.